sustainability

MDPI

Article

Hematite/Graphitic Carbon Nitride Nanofilm for Fenton and Photocatalytic Oxidation of Methylene Blue

Sangbin Lee and Jae-Woo Park *

Department of Civil and Environmental Engineering, Hanyang University, Seoul 04763, Korea; sangbinlee@hanyang.ac.kr

* Correspondence: jaewoopark@hanyang.ac.kr; Tel.: +82-2-2220-1483

Received: 18 March 2020; Accepted: 2 April 2020; Published: 3 April 2020

Abstract: Hematite (α-Fe_2O_3)/graphitic carbon nitride (g-C_3N_4) nanofilm catalysts were synthesized on fluorine-doped tin oxide glass by hydrothermal and chemical vapor deposition. Scanning electron microscopy, energy-dispersive spectroscopy, X-ray diffraction, and X-ray photoelectron spectroscopy analyses of the synthesized catalyst showed that the nanoparticles of g-C_3N_4 were successfully deposited on α-Fe_2O_3 nanofilm. The methylene blue degradation efficiency of the α-Fe_2O_3/g-C_3N_4 composite catalyst was 2.6 times greater than that of the α-Fe_2O_3 single catalyst under ultraviolet (UV) irradiation. The methylene blue degradation rate by the α-Fe_2O_3/g-C_3N_4 catalyst increased by 6.5 times after 1 mM of hydrogen peroxide (H_2O_2) was added. The photo-Fenton reaction of the catalyst, UV, and H_2O_2 greatly increased the methylene blue degradation. The results from the scavenger experiment indicated that the main reactants in the methylene blue decomposition reaction are superoxide radicals photocatalytically generated by g-C_3N_4 and hydroxyl radicals generated by the photo-Fenton reaction. The α-Fe_2O_3/g-C_3N_4 nanofilm showed excellent reaction rate constants at pH 3 ($K_a = 6.13 \times 10^{-2}$ min^{-1}), and still better efficiency at pH 7 ($K_a = 3.67 \times 10^{-2}$ min^{-1}), compared to other methylene blue degradation catalysts. As an immobilized photo-Fenton catalyst without iron sludge formation, nanostructured α-Fe_2O_3/g-C_3N_4 are advantageous for process design compared to particle-type catalysts.

Keywords: hematite; graphitic carbon nitride; photocatalyst; heterojunction; photo-Fenton

1. Introduction

Advanced oxidation processes (AOPs) include various methods of decomposing organics through the generation of reactive oxygen species (ROS), such as hydroxyl radicals (•OH) or superoxide radicals ($\bullet O_2^-$) [1], which are intermediate reactants with strong oxidizing power. AOPs include the Fenton reaction, ozone (O_3)/hydrogen peroxide (H_2O_2), ultraviolet (UV)/H_2O_2, UV/O_3, and photocatalysis. Photocatalysis is promising because of its environmental stability, low processing costs, and wide applications [2]. Photocatalysts are semiconductors that can excite electrons with light energy and form hole–electron pairs. The excited electrons and generated holes are decomposed directly or indirectly by ROS generation through redox reactions. The energy levels in the valence and conduction bands where holes and electrons are present are important factors in photocatalytic activity. They determine the oxidizable organics and the ROS that can be produced depending on the redox potential. Another important factor in the development of photocatalytic processes is the bandgap energy, which is the difference between energy levels of the valence and conduction bands. Photocatalysts are activated by light with energy above the bandgap, and the energy of light is related to the wavelength of light available. Lower bandgaps have a wider spectrum of available light.

The Fenton process is a widely used AOP for water treatment, as it is inexpensive. It can be carried out at room temperature and low atmospheric pressure. In the Fenton reaction, ferric ions react with $H_2O_2$to form ROS species that oxidize organic matter as shown in Equation (1).

$$Fe^{2+} + H_2O_2 \rightarrow Fe^{3+} + OH^- + \bullet OH. \quad (1)$$

One disadvantage of the Fenton process is that H_2O_2 consumes radicals and wastes oxidizing agents, reducing oxidation efficiency. The other disadvantage is the loss of Fe ions and the formation of solid sludge. The photo-Fenton process, which combines UV with traditional Fenton reactions, is an alternative to the conventional Fenton process that increases oxidation efficiency and reduces sludge. The combination of UV with the Fenton process was reported to significantly reduce iron loss and sludge production [3]. The additional reaction by UV, as shown in Equations (2) and (3), allows the photo-Fenton process to generate more ROS than the simple Fenton process.

$$Fe(OH)_2{}^+ + hv \rightarrow Fe^{2+} + 2OH^-, \quad (2)$$

$$H_2O_2 + hv \rightarrow 2\bullet OH. \quad (3)$$

Hematite (α-Fe_2O_3) can be used as a photocatalyst with a bandgap of 2.2 eV and also can be used as a catalyst for the Fenton reaction by the change of Fe ions on its surface. By combining α-Fe_2O_3 with H_2O_2 and UV, photocatalytic reactions can be carried out simultaneously. However, existing hematite-based photocatalysts exhibit high hole–electron recombination due to the narrow bandgap and limited ROS production. This is because of the low redox potential of the conduction band; as a result, it is not practical to apply to water treatment. To overcome these shortcomings, various modification studies have been carried out, testing non-metal doping [4,5], metal doping [6–8], shape control [9–11], and heterojunction [12–14]. A heterojunction with other catalysts accumulates charge and reduces hole–electron recombination by moving excited electrons to the energy levels of other catalysts through the interaction of two semiconductors with different band structures. Graphitic carbon nitride (g-C_3N_4) has a relatively low bandgap energy and enough conduction band potential for $\bullet O_2{}^-$ generation, making it suitable as a junction catalyst for α-Fe_2O_3 modification.

Nanostructured α-Fe_2O_3 has been studied to be used as a catalyst for the Fenton reaction. Guo et al. [15] confirmed that S-doped α-Fe_2O_3 exhibited excellent heterogeneous Fenton efficiency under UV/visible light, while little Fenton reactivity was observed in the dark. Liao et al. [16] reported that phenol and phenolic contaminants were decomposed using an α-Fe_2O_3 catalyst supported on multiwall carbon nanotubes, showing 20% higher degradation efficiency than bare α-Fe_2O_3. Chan et al. [17] reported that exposed surface facets play an important role in determining catalytic performance in methylene blue degradation with nanostructured α-Fe_2O_3. It was confirmed that the photocatalytic performance of three types of α-Fe_2O_3 nanoparticles was in the order of {113}> {104}> {001}. Liu et al. [18] reported that the increase in sintering temperature of α-Fe_2O_3 nanoparticles increased in methylene decomposition. They used α-Fe_2O_3 nanoparticles synthesized by a simple sodium dodecyl sulfate-assisted grinding reaction and subsequent heating treatment process. The α-Fe_2O_3 particles obtained at 500 °C showed the highest decomposition efficiency. Liu et al. [19] synthesized nanoring-type α-Fe_2O_3 by adding H_2PO_4, $SO_4{}^{2-}$, and citric acid in a hydrothermal reaction and reported increased photo-Fenton decomposition of p-nitrophenol by activating photoabsorption and increasing surface-coupled Fe^{2+} content. Jiang et al. [20] reported that α-Fe_2O_3/BiOI catalysts showed 3 and 10 times higher decomposition efficiency than BiOI and α-Fe_2O_3 catalysts in methyl orange, phenol, and tetracycline hydrochloride decomposition. The interaction of the two catalysts increases the separation and transfer efficiency of photogenerated charges and results in an optimized Fenton reaction at the solid–liquid interface. Ren et al. [21] reported that Cu-doping interacted with α-Fe_2O_3 to have higher Fenton activity than undoped samples in methylene blue degradation. The previous studies show that nanostructured α-Fe_2O_3 can be used in the Fenton reaction and can increase the activity of the catalyst through shape control and doping. However, there are inherent limitations in the process design of nanoparticle-type catalysts. They require a separate catalyst recovery process

after contaminant treatment. This may reduce the merits of decreased sludge generation by using α-Fe_2O_3, which is advantageous compared to the Fenton reaction using iron salt. The α-Fe_2O_3 catalyst with nanostructures in an immobilized form rather than in particle form can be easier to use and decrease the costs of process design and operation.

The α-Fe_2O_3 also is being actively studied as a photocatalyst. However, due to its low photoactivity when used alone, it is often used in heterojunction with other catalysts. The g-C_3N_4 is frequently used with α-Fe_2O_3 because of their band structures. It acts as a Z-scheme photocatalyst with the band of α-Fe_2O_3 and can produce $\bullet O_2^-$, that cannot be produced by α-Fe_2O_3. Bai et al. [22] reported that α-Fe_2O_3 and porous g-C_3N_4 composites (K_a = 1.28×10^{-1} min^{-1}) showed 1.43 times better efficiency than pure g-C_3N_4 (ka = 5.64 × 10^{-2} min^{-1}) in the degradation of Rhodamine B. Sun et al. [23] found that the α-Fe_2O_3/g-C_3N_4 heterojunction photocatalyst (K_a = 4.70 × 10^{-3} min^{-1}) showed increases of 11.8 and 5.9 times in arsenic removal efficiency relative to pure α-Fe_2O_3 and g-C_3N_4, respectively. Hao et al. [24] reported that 55% of methylene blue was removed in a 180 min reaction with g-C_3N_4 alone, while 75% of methylene blue was removed after 180 min with the α-Fe_2O_3/g-C_3N_4 complex photocatalyst. In the charge transfer characterization using electrochemical impedance spectroscopy and photocurrent, α-Fe_2O_3/g-C_3N_4 has a smaller charge transfer resistance and higher photocurrent response than g-C_3N_4. Zhou et al. [25] confirmed that the photo-Fenton reaction using the α-Fe_2O_3/g-C_3N_4 catalyst was 45.4 times and 8.4 times more efficient than those of pure α-Fe_2O_3 and g-C_3N_4, respectively. It also was 7.2 times more efficient than a mixture of the two catalysts. However, its potential as a Fenton catalyst was seldom utilized, as most studies focused on the use of α-Fe_2O_3 as a photocatalyst.

In this study, we synthesized a nanostructured α-Fe_2O_3/g-C_3N_4 catalyst on a fluorine-doped tin oxide (FTO) glass. The α-Fe_2O_3/g-C_3N_4 catalyst simultaneously acts as a photocatalyst and photo-Fenton catalyst. Catalysts immobilized on FTO glass have advantages in process design because they reduce the loss of iron ions and do not require a separate recovery process. A junction with g-C_3N_4 enables the use of more ROS species while improving the photoelectrochemical properties of the catalyst.

2. Experimental Section

2.1. Materials Synthesis

Nanostructured α-Fe_2O_3 films were synthesized on FTO glass simply by a modified hydrothermal method [26]. As a precursor for synthesizing α-Fe_2O_3 nanofilms, 10 mM $FeCl_3 \bullet 6H_2O$ and $NaNO_3$ were dissolved in 100 mL of 0.05 M HCl solution. The solution was put in a 150 mL Teflon liner. A piece of FTO glass ultrasonicated in acetone, ethanol, and distilled water was placed on the Teflon liner. Next, the Teflon liner was placed in a stainless-steel autoclave and heated at 95 °C for 4 h in an electric furnace. Akaganeite(β-FeOOH) films were successfully synthesized on the FTO glass. The obtained β-FeOOH films were washed with distilled water and sintered in an electric furnace at 520 °C for 2 h, resulting in the synthesis of red-colored α-Fe_2O_3 films.

The g-C_3N_4 was synthesized on α-Fe_2O_3 nanofilms by directly heating melamine [27]. First, 5 g of melamine was placed in a ceramic crucible with a cover. Then, the β-FeOOH films were placed on the melamine with β-FeOOH facing down. The crucible was partially covered and heated at 520 °C for 2 h in an electric furnace. The sample was then cooled to room temperature in the atmosphere. After the reaction, brick-colored α-Fe_2O_3/g-C_3N_4 films were obtained with yellow g-C_3N_4 powders on the bottom of the crucible. It was confirmed that 280 mg of catalyst was synthesized on one FTO substrate by comparing the weight before and after synthesis.

2.2. Materials Characterization

The morphology and nanostructures of the samples were analyzed by field-emission scanning electron microscopy (FE-SEM; JSM-6701F and FEI Nova NanoSEM 450, JEOL, Japan). Energy-dispersive spectroscopy (EDS) was used for surface elemental analysis using the FE-SEM. To analyze the crystal

phase, X-ray diffraction (XRD; SmartLab, Rigaku, Japan) analysis was carried out with Cu kα radiation. XRD data were obtained at conditions of 45 kV, 200 mA, from 2θ = 20° to 80°, with a step size of 0.04° at 4°/min. X-ray photoelectron spectroscopy (XPS; K-alpha plus, Thermo Scientific, Massachusetts, US) was taken with Al kα (1486.6 eV).

2.3. Aqueous Organic Oxidation

The organic oxidation efficiency of the sample was confirmed by methylene blue decomposition. The sample was placed in a 250 mL quartz beaker and 200 mL of 10 mg/L methylene blue solution was added. The beaker was placed in a reactor with three UV lamps (254 nm, 6 W) and irradiated with light for the reaction for 90 min. The light intensity applied to the center of the catalyst was 2.88 mW/cm^2. It was measured using a lux meter (UVC-254SD, Lutron Electronics, Pennsylvania, US). During the reaction, the solution was stirred with an electric stirrer. Experiments were also carried out under the same conditions with addition of various concentrations of H_2O_2 (0.1, 0.2, 0.5, 1, and 2 mM) and pH (3, 5, 7, 9, and 11). Scavenger experiments were performed to measure the main reactants of the methylene blue degradation. The methylene blue degradations after addition of 1 mM benzoquinone (BQ) or tert-butyl alcohol (TBA) were compared after 90 min of reactions at the initial pH 7. A total of 4 mL of the solution was collected at regular intervals and filtered using a syringe filter (pore size: 0.45 μm, Whatman, UK). The filtered samples were analyzed by examining the absorbance of 665 nm light by a UV-vis spectrometer (DR 2800, HACH, Colorado, US) to determine the methylene blue degradation rate. All experimental data were duplicated and averaged.

3. Results and Discussion

3.1. Structural Analysis

Figure 1 shows the morphology and nanostructures of (a) β-FeOOH and (b) α-Fe_2O_3. The FeOOH has nanorods arranged like flowers. The nanorods are about 50 nm wide and angled. The nanostructure of α-Fe_2O_3 changed to a more rounded form after sintering, and both the width and length were smaller than those of the β-FeOOH nanorods. This change is due to the escape of H_2O when β-FeOOH is sintered and α-Fe_2O_3 is formed, as shown in Equation (4) [28].

$$2FeOOH \rightarrow Fe_2O_3 + H_2O \quad (4)$$

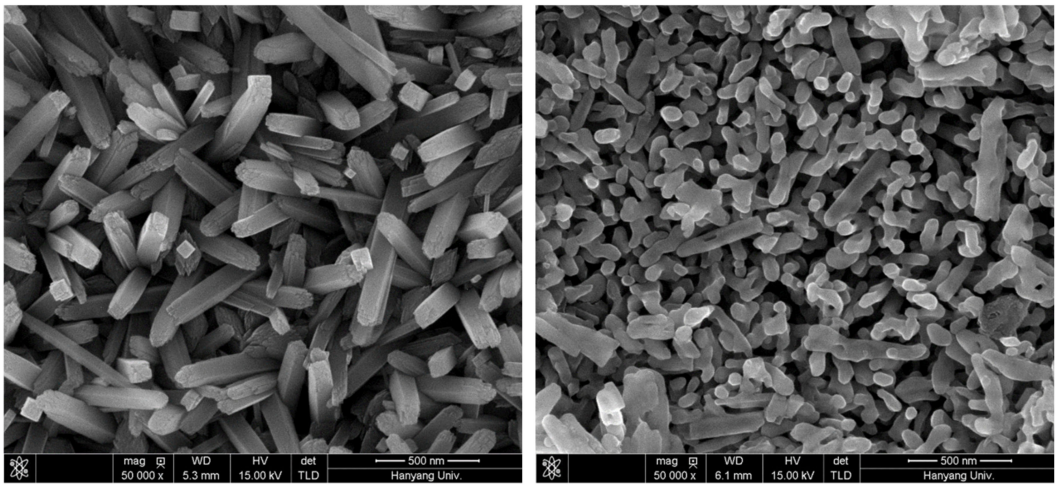

(**a**) (**b**)

Figure 1. Scanning electron microscopy (SEM) image of nanostructure of (**a**) β-FeOOH and (**b**) α-Fe_2O_3.

Figure 2 shows the FE-SEM image and EDS analysis of the α-Fe_2O_3/g-C_3N_4 films. The particles of g-C_3N_4 were deposited on the α-Fe_2O_3 nanostructures. The g-C_3N_4 particles are less than 35 nm in size, and the shape of Fe_2O_3 is rounder due to further sintering. The C, N, Fe, and O peaks were identified in EDS analysis. The peaks of elements other than O were measured slightly lower because the analysis depth of EDS is greater than the thickness of α-Fe_2O_3/g-C_3N_4 films. As a result, the elements of the FTO under the catalyst are also measured. The peaks between 3 and 4 keV correspond to Sn, which is a component of FTO.

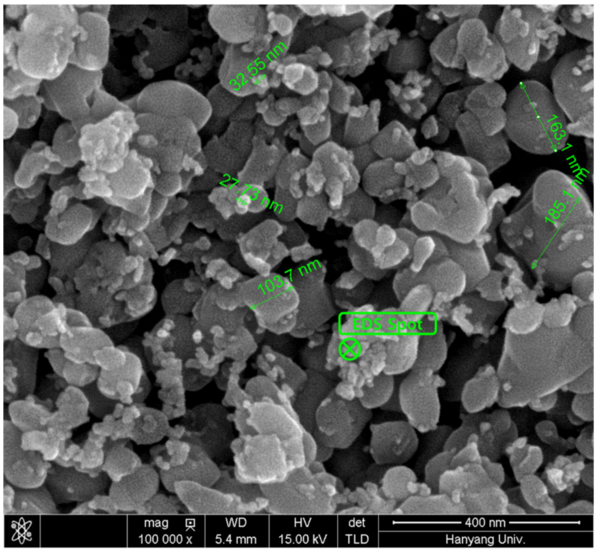

(**a**)

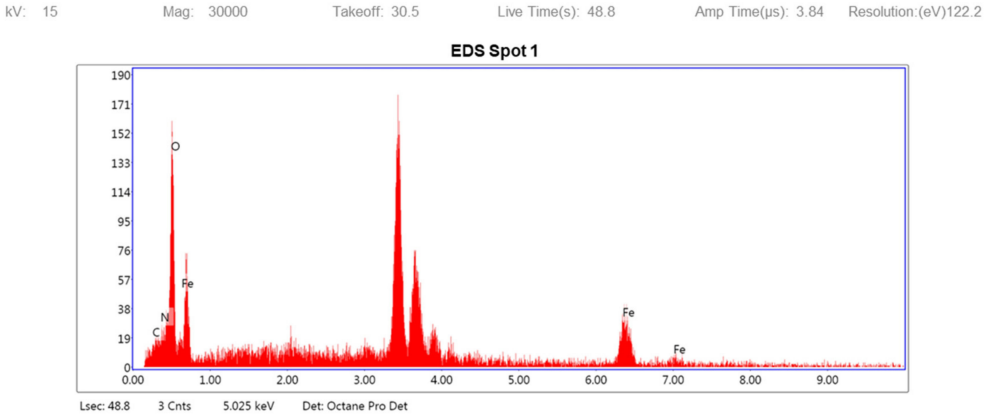

eZAF Smart Quant Results

Element	Weight %	Atomic %	Net Int.	Error %	Kratio	Z	R	A	F
C K	12.04	19.08	7.25	15.63	0.0516	1.1154	0.9420	0.3838	1.0000
N K	17.90	24.32	8.90	16.78	0.0660	1.0879	0.9537	0.3389	1.0000
O K	38.56	45.86	35.56	11.77	0.1253	1.0639	0.9640	0.3055	1.0000
FeK	31.50	10.74	18.22	11.75	0.2634	0.7969	1.0548	1.0116	1.0372

(**b**)

Figure 2. (**a**) SEM image and (**b**) energy-dispersive spectroscopy (EDS) spectrum of α-Fe_2O_3/g-C_3N_4 nanofilm.

Figure 3 shows the XRD patterns of β-FeOOH, α-Fe_2O_3, and α-Fe_2O_3/g-C_3N_4 samples and bare FTO. The peak of FeOOH was observed on the FTO substrate after the hydrothermal synthesis. After

sintering, FeOOH was successfully converted to α-Fe_2O_3, and the eight characteristic peaks of α-Fe_2O_3 ({012}, {104}, {110}, {113}, {024}, {116}, {214}, and {300}) were observed [29]. The peaks of the FTO glass were also observed in the samples due to the thinness of the α-Fe_2O_3 film layer. No characteristic peaks of g-C_3N_4 were observed in the α-Fe_2O_3/g-C_3N_4 samples, and only the peaks of α-Fe_2O_3 and FTO were identified. This may be because the amount of g-C_3N_4 deposited on the surface is relatively small, and it is dispersed well on the surface without affecting the structure of α-Fe_2O_3.

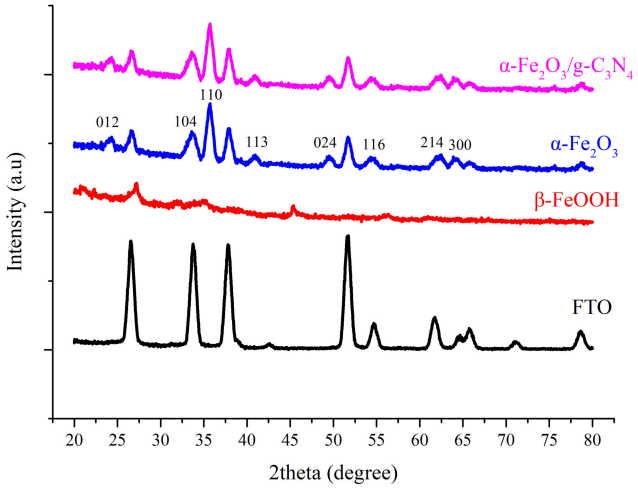

Figure 3. X-ray diffraction (XRD) pattern of bare fluorine-doped tin oxide (FTO), β-FeOOH, α-Fe_2O_3, and α-Fe_2O_3/g-C_3N_4.

XPS analysis was performed to confirm the synthesis of g-C_3N_4. Figure 4 shows (a) the XPS spectrum of α-Fe_2O_3/g-C_3N_4 and the (b) C 1s and (c) N 1s regions. Four elements (Fe, O, C, and N) were detected in the XPS spectra. The most prominent peak in the C 1s region is attributed to the carbon–nitrogen bond structure (N-C = N) of the aromatic systems. The peak at 398.3 eV seen in the N 1s region is the peak attributed to graphene N and generally indicates the case where the nitrogen atom is incorporated into the graphene layer to replace the carbon atom. The peak at 401.0 eV is attributed to nitrogen spiked with three sp^2 carbon atoms [30,31]. The peaks in the C 1s and N 1s regions show that the melamine produced g-C_3N_4 with a graphitic structure through heating and was successfully deposited on the α-Fe_2O_3 surface.

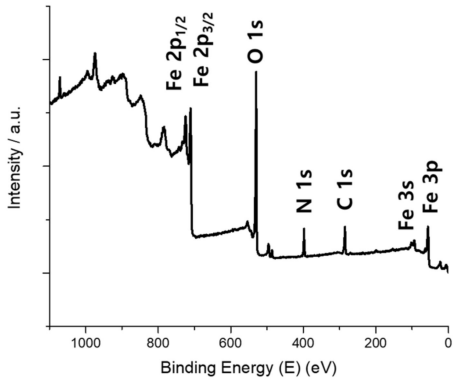

(**a**)

Figure 4. *Cont.*

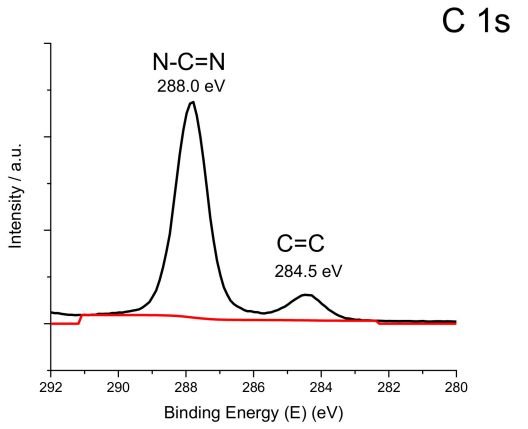

(**b**)

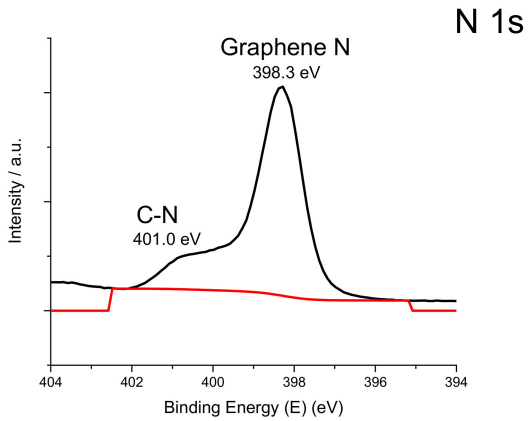

(**c**)

Figure 4. X-ray photoelectron spectroscopy (XPS) spectra of (**a**) whole surface, and (**b**) C1s and (**c**) N1s regions of the α-Fe_2O_3/g-C_3N_4.

3.2. Methylene Blue Degradation

Methylene blue degradation results are shown in Figure 5. No significant changes were observed when the experiment was performed using bare FTO glass. Only 12% of methylene blue was degraded with pure α-Fe_2O_3 after the 90 min reaction even under UV irradiation, whereas 31% of methylene blue was degraded with the α-Fe_2O_3/g-C_3N_4 heterojunction catalyst. This is because the band structure of α-Fe_2O_3, which cannot generate $\bullet O_2^-$, is not suitable for methylene blue decomposition, whereas the conduction band of g-C_3N_4 has enough redox potential for $\bullet O_2^-$ production. In the decomposition of photocatalytic organic matter of α-Fe_2O_3/g-C_3N_4, g-C_3N_4 can be said to be the main catalyst, as opposed to α-Fe_2O_3.

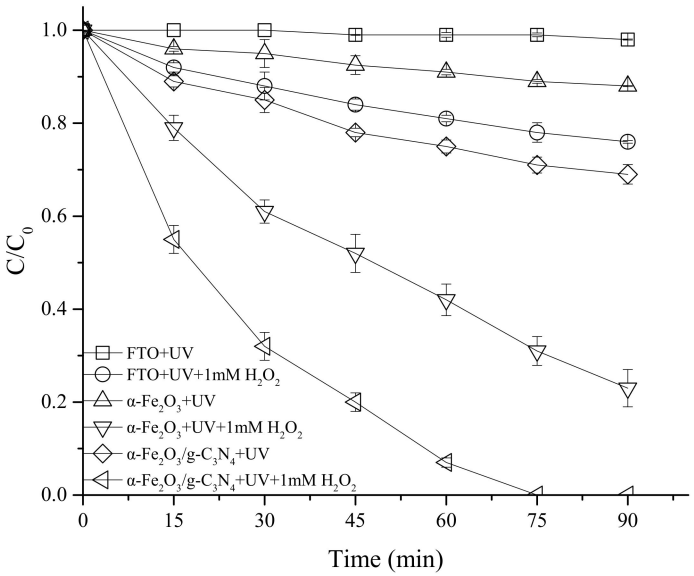

Figure 5. The degradation of methylene blue in different catalytic systems.

After addition of 1 mM H_2O_2, the methylene blue degradation rate increased significantly in all samples. The increase in methylene blue degradation rate in bare FTO samples was due to the UV/H_2O_2 reaction, and the increases in degradation efficiency due to H_2O_2 addition in α-Fe_2O_3 and α-Fe_2O_3/g-C_3N_4 samples were greater than that by the UV/H_2O_2 reaction. This means that there is an interaction between the α-Fe_2O_3 and α-Fe_2O_3/g-C_3N_4 catalyst and H_2O_2 in addition to the UV/H_2O_2 reaction. The methylene blue degradation rate of the α-Fe_2O_3 catalyst under UV irradiation increased from 12% to 77% with H_2O_2 addition after 90 min of reaction. Methylene blue degradation of α-Fe_2O_3/g-C_3N_4 showed 31% degradation efficiency after 90 min of reaction under UV irradiation, but after H_2O_2 addition, the complete decomposition of methylene blue was achieved in only 75 min of reaction. This is due to the Fenton reaction, in which the Fe^{3+} on the surface of α-Fe_2O_3 becomes Fe^{2+} due to the excited α-Fe_2O_3 electrons under UV light. They, in turn, reacted with H_2O_2 to form •OH [17,32].

The change of methylene blue decomposition efficiency caused by the concentration of H_2O_2 added is shown in Figure 6. For H_2O_2 concentrations of up to 1 mM, the higher the concentration of the H_2O_2 added, the higher the decomposition efficiency will be. However, no noticeable change in efficiency was seen at 1 and 2 mM. This may be due to the saturation of the number of surface Fe ions reacting with H_2O_2 at 1 mM H_2O_2. The effect of the initial pH is presented in Figure 7. At low initial pH concentrations, the methylene blue decomposition efficiency was increased. This optimal pH is similar to those of the Fenton process. This shows that the α-Fe_2O_3/g-C_3N_4 catalyst performs both Fenton and photocatalytic oxidation simultaneously.

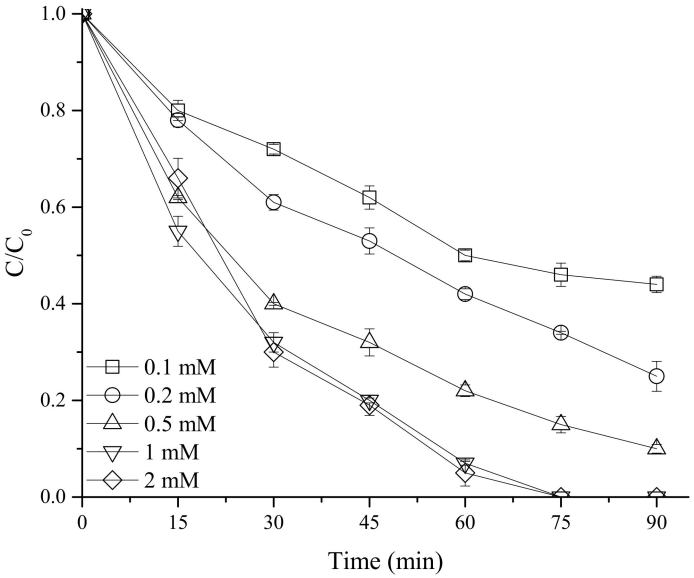

Figure 6. Methylene blue degradation of α-Fe_2O/g-C_3N_4 nanofilm with addition of different concentrations of H_2O_2.

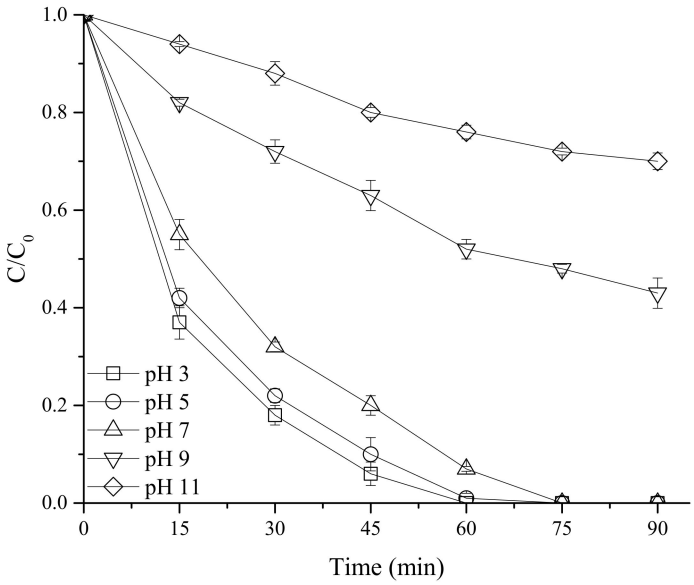

Figure 7. Methylene blue decomposition of α-Fe_2O_3/g-C_3N_4 nanofilm with different initial pH.

3.3. Detection of Reactive Species

ROS scavengers were added to the methylene blue oxidation to identify the main reactants. BQ was introduced as an $\bullet O_2^-$ scavenger, and TBA was used as an •OH scavenger [33]. As shown in Figure 8, the effect of the •OH scavenger was low without H_2O_2 addition. On the other hand, when the $\bullet O_2^-$ scavenger was added, the reaction was significantly inhibited. This means that, in the absence of H_2O_2, the main reactant of methylene blue oxidation is the $\bullet O_2^-$ produced in the conduction band of g-C_3N_4. However, when H_2O_2 assists in oxidation, the degradation rate was significantly lowered when •OH scavenger was added. This shows that the •OH generated by the Fenton reaction is one of the major reactants in the methylene blue decomposition reaction.

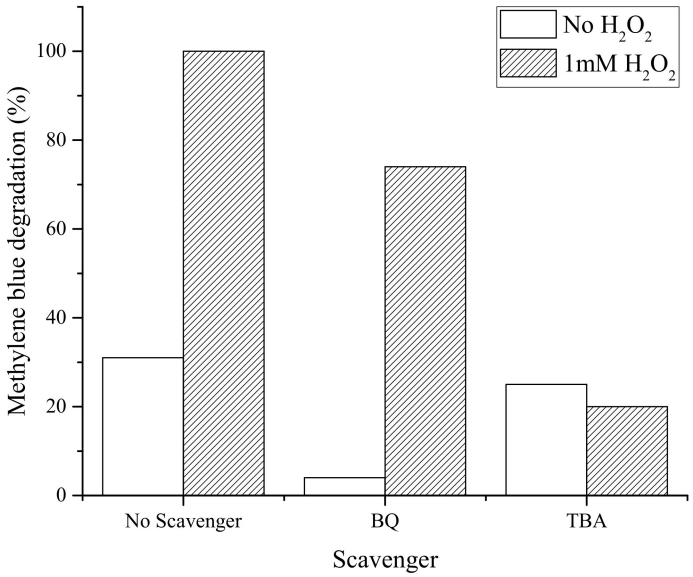

Figure 8. Methylene blue photodegradation efficiency of α-Fe_2O_3/g-C_3N_4 nanofilm with different radical scavengers.

3.4. Degradation Kinetics

The methylene blue degradation during the first 45 min of this study can be explained by the pseudo-first-order reaction kinetics of Equation (5).

$$\ln (C_0/C) = K_a \times t + \text{constant}, \quad (5)$$

where C_0 is the initial concentration of methylene blue, C is the methylene blue concentration at time t, and K_{app} is the first-order reaction constant. K_a was chosen as a kinetic parameter to compare the catalytic activity of different systems independently of concentration. Kinetic parameters for each methylene blue degradation process are listed in Tables 1 and 2. All results followed a linear regression and K_a effectively expressed the methylene blue decomposition efficiency. The reaction rate of α-Fe_2O_3/g-C_3N_4 nanofilm was 2.4 times higher than that of theα-Fe_2O_3 film under conditions of pH 7 and 1 mM H_2O_2 concentration, and the methylene blue decomposition rate of α-Fe_2O_3/g-C_3N_4 nanofilms at the initial pH 3 increased by 67% over that at pH 7. Previous studies on methylene blue degradation are listed in Table 3, demonstrating that α-Fe_2O_3/g-C_3N_4 nanofilms are excellent even in neutral conditions.

Table 1. Kinetic parameters of different methylene blue decomposition systems in this study.

Type of Oxidation Process	K_a (min^{-1})	R^2
FTO + UV	1.40×10^{-4}	0.99
α-Fe_2O_3 + UV	1.80×10^{-3}	0.99
α-Fe_2O_3/g-C_3N_4 + UV	5.65×10^{-3}	0.99
FTO + UV + H_2O_2	4.11×10^{-3}	0.99
α-Fe_2O_3 + UV + H_2O_2	1.52×10^{-2}	0.99
α-Fe_2O_3/g-C_3N_4 + UV + H_2O_2	3.67×10^{-2}	0.99

Table 2. Kinetic parameters of the methylene blue degradation of α-Fe_2O_3/g-C_3N_4 nanofilm according to concentration of added H_2O_2 and initial pH.

H_2O_2 (mM)	pH	K_a (min^{-1})	R^2
0.1	7	1.10×10^{-2}	0.99
0.2	7	1.50×10^{-2}	0.99
0.5	7	2.73×10^{-2}	0.99
1	7	3.67×10^{-2}	0.99
2	7	3.72×10^{-2}	0.99
1	3	6.13×10^{-2}	0.99
1	5	5.15×10^{-2}	0.99
1	9	1.07×10^{-2}	0.99
1	11	4.70×10^{-3}	0.99

Table 3. Comparison of K_{app} values of previous studies of methylene blue degradation.

Catalyst	K_a (/min)	Light Source	Reference
TiO_2–curcumin	3.05×10^{-2}	UV	[34]
Cu doped ZnS	1.45×10^{-2}	UV	[35]
ZIF-8	1.70×10^{-2}	UV	[36]
TiO_2/rGO nanocomposites	1.12×10^{-2}	UV	[37]
CA/TPNC	1.26×10^{-2}	Solar	[38]
TiO_2/graphene	2.08×10^{-2}	Solar	[39]
TiO_2 NRAs/graphene/ZnO NPs	1.65×10^{-2}	Visible	[40]
(Mo,C)-TiO_2/FTO	2.95×10^{-2}	Visible	[41]
g-C_3N_4-10RGO-TiO_2	1.47×10^{-2}	Visible	[42]
This study (1mM H_2O_2, pH 7)	3.67×10^{-2}	UV	-
This study (1mM H_2O_2, pH 3)	6.13×10^{-2}	UV	-

3.5. Methylene Blue Degradation Mechanism

The degradation mechanism of the catalyst based on these results is shown in Figure 9. Traditional dual-carrier delivery systems, shown in Figure 9a, cannot account for the high activity of $\bullet O_2^-$ in reactions without H_2O_2. When the redox potential for generating the $\bullet O_2^-$ is −0.046 (eV vs. normal hydrogen electrode) and the electrons move to the conduction band of α-Fe_2O_3, the photocatalytic activity is somewhat lower [43]. The holes and electrons accumulated due to the Z-scheme process of α-Fe_2O_3/g-C_3N_4 can be used for photocatalytic oxidation, as shown in Figure 9b. The Z-scheme action of the α-Fe_2O_3/g-C_3N_4 heterojunction catalyst in the field of electrolysis and CO_2 reduction has been reported [44–46]. However, the activity of low •OH in the absence of H_2O_2 cannot be explained with the Z-scheme system. If the •OH is produced in the valence band of α-Fe_2O_3, there should be enough •OH activity even without H_2O_2. Thus, the combination of photocatalytic and Fenton processes is presented in Figure 9c. The high activity of •OH in the presence of H_2O_2 means that •OH involved in photodegradation is generated in H_2O_2. The electrons excited by UV can change Fe^{3+} to Fe^{2+} on the α-Fe_2O_3 surface, and Fe^{2+} reacts with H_2O_2 to generate •OH [32,47]. The difference in the energy levels of g-C_3N_4 and α-Fe_2O_3 induces charge transfer. The junctions of two semiconductors with different band structures can accumulate charge by shifting the photoexcited electrons to the energy levels of the other catalysts. The coupled g-C_3N_4 valence band acts as an electron trap for electrons excited by the conduction band of α-Fe_2O_3. Catalysts composed of highly efficient nanostructures have low electron resistance, and the heterojunction structures of both catalysts make charge separation more efficient and reduce hole–electron recombination caused by instability of excited electrons.

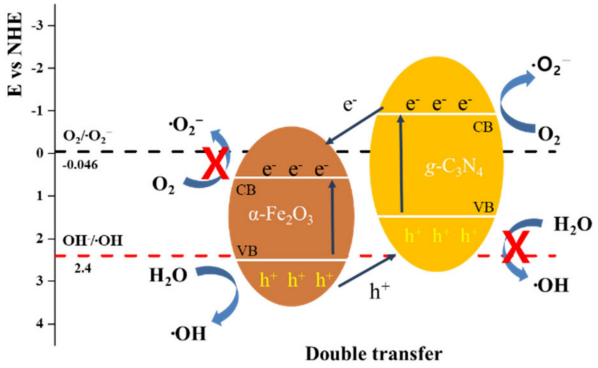

(**a**)

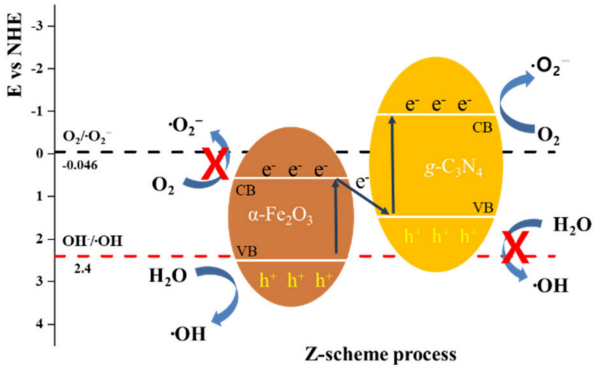

(**b**)

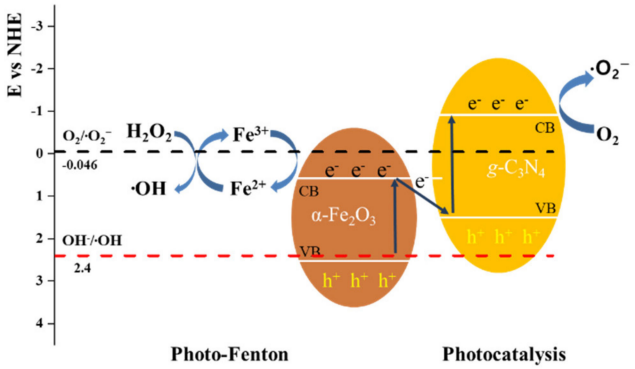

(**c**)

Figure 9. Schematic diagrams of charge transfer between g-C_3N_4 and α-Fe_2O_3 with the radical generation processes: (**a**) double transfer, (**b**) Z-scheme, and (**c**) combination of photo-Fenton and photocatalysis.

4. Conclusions

Nano-structured α-Fe_2O_3 was successfully synthesized on FTO glass. Nanoparticles of g-C_3N_4 were successfully deposited on the synthesized α-Fe_2O_3 films. In the methylene blue oxidation using α-Fe_2O_3/g-C_3N_4 nanofilm, the activity of •OH under UV irradiation was low when H_2O_2 was not present. XPS analysis showed changes in Fe ions on the α-Fe_2O_3 surface by H_2O_2, which is similar to the change in iron ions in the Fenton reaction. The Fenton reaction of iron ions on the surface

of α-Fe_2O_3 activated by H_2O_2 and the photocatalytic activity of g-C_3N_4 nitride enhanced through heterojunction with α-Fe_2O_3 are suggested as the main mechanisms of α-Fe_2O_3/g-C_3N_4 nanofilms. The α-Fe_2O_3/g-C_3N_4 nanofilms as immobilized Fenton-photocatalytic composite catalysts are advantageous for reactor design as an alternative to conventional treatment with iron salts.

Author Contributions: Conceptualization, S.L.; Data curation, S.L.; Formal analysis, S.L.; Methodology, S.L. and J.-W.P.; Supervision, J.-W.P.; Visualization, S.L.; Writing—original draft, S.L.; Writing—review & editing, J.-W.P. All authors have read and agreed to the published version of the manuscript.

Funding: This research was supported by the Korea Environmental Industry and Technology Institute (KEITI) through The Chemical Accident Prevention Technology Development Project, funded by Korea Ministry of Environment (MOE) (2019001960005).

Conflicts of Interest: The authors declare no conflict of interest.

References

1. Pera-Titus, M.; García-Molina, V.; Baños, M.A.; Giménez, J.; Esplugas, S. Degradation of chlorophenols by means of advanced oxidation processes: A general review. *Appl. Catal. B Environ.* **2004**, *47*, 219–256. [CrossRef]
2. Chong, M.N.; Jin, B.; Chow, C.W.K.; Saint, C. Recent developments in photocatalytic water treatment technology: A review. *Water Res.* **2010**, *44*, 2997–3027. [CrossRef] [PubMed]
3. Rahim Pouran, S.; Abdul Aziz, A.R.; Wan Daud, W.M.A. Review on the main advances in photo-Fenton oxidation system for recalcitrant wastewaters. *J. Ind. Eng. Chem.* **2015**, *21*, 53–69. [CrossRef]
4. Pradhan, G.K.; Sahu, N.; Parida, K.M. Fabrication of S, N co-doped α-Fe_2O_3 nanostructures: Effect of doping, OH radical formation, surface area, [110] plane and particle size on the photocatalytic activity. *RSC Adv.* **2013**, *3*, 7912–7920. [CrossRef]
5. He, L.; Jing, L.; Luan, Y.; Wang, L.; Fu, H. Enhanced Visible Activities of α-Fe_2O_3 by Coupling N-Doped Graphene and Mechanism Insight. *ACS Catal.* **2014**, *4*, 990–998. [CrossRef]
6. Li, F.B.; Li, X.Z.; Liu, C.S.; Liu, T.X. Effect of alumina on photocatalytic activity of iron oxides for bisphenol A degradation. *J. Hazard. Mater.* **2007**, *149*, 199–207. [CrossRef]
7. Chen, L.; Li, F.; Ni, B.; Xu, J.; Fu, Z.; Lu, Y. Enhanced visible photocatalytic activity of hybrid Pt/α-Fe_2O_3 nanorods. *RSC Adv.* **2012**, *2*, 10057–10063. [CrossRef]
8. Cao, S.-W.; Fang, J.; Shahjamali, M.M.; Wang, Z.; Yin, Z.; Yang, Y.; Boey, F.Y.C.; Barber, J.; Loo, S.C.J.; Xue, C. In situ growth of Au nanoparticles on Fe_2O_3 nanocrystals for catalytic applications. *CrystEngComm* **2012**, *14*, 7229–7235. [CrossRef]
9. Kawahara, T.; Yamada, K.; Tada, H. Visible light photocatalytic decomposition of 2-naphthol by anodic-biased α-Fe_2O_3 film. *J. Colloid Interface Sci.* **2006**, *294*, 504–507. [CrossRef]
10. Tamboli, S.H.; Rahman, G.; Joo, O.-S. Influence of potential, deposition time and annealing temperature on photoelectrochemical properties of electrodeposited iron oxide thin films. *J. Alloy. Compd.* **2012**, *520*, 232–237. [CrossRef]
11. Zhang, Z.; Hossain, M.F.; Takahashi, T. Self-assembled hematite (α-Fe_2O_3) nanotube arrays for photoelectrocatalytic degradation of azo dye under simulated solar light irradiation. *Appl. Catal. B Environ.* **2010**, *95*, 423–429. [CrossRef]
12. Jaramillo-Páez, C.; Navío, J.A.; Hidalgo, M.C.; Bouziani, A.; Azzouzi, M.E. Mixed α-Fe_2O_3/Bi_2WO_6 oxides for photoassisted hetero-Fenton degradation of Methyl Orange and Phenol. *J. Photochem. Photobiol. A Chem.* **2017**, *332*, 521–533. [CrossRef]
13. Sarkar, D.; Singh, A.K. Mechanism of Nonvolatile Resistive Switching in ZnO/α-Fe_2O_3 Core–Shell Heterojunction Nanorod Arrays. *J. Phys. Chem. C* **2017**, *121*, 12953–12958. [CrossRef]
14. Kang, J.; Kuang, Q.; Xie, Z.-X.; Zheng, L.-S. Fabrication of the SnO_2/α-Fe_2O_3 Hierarchical Heterostructure and Its Enhanced Photocatalytic Property. *J. Phys. Chem. C* **2011**, *115*, 7874–7879. [CrossRef]
15. Guo, L.; Chen, F.; Fan, X.; Cai, W.; Zhang, J. S-doped α-Fe_2O_3 as a highly active heterogeneous Fenton-like catalyst towards the degradation of acid orange 7 and phenol. *Appl. Catal. B Environ.* **2010**, *96*, 162–168. [CrossRef]
16. Liao, Q.; Sun, J.; Gao, L. Degradation of phenol by heterogeneous Fenton reaction using multi-walled carbon nanotube supported Fe_2O_3 catalysts. *Colloids Surf. A Physicochem. Eng. Asp.* **2009**, *345*, 95–100. [CrossRef]

17. Chan, J.Y.T.; Ang, S.Y.; Ye, E.Y.; Sullivan, M.; Zhang, J.; Lin, M. Heterogeneous photo-Fenton reaction on hematite (α-Fe_2O_3){104}, {113} and {001} surface facets. *Phys. Chem. Chem. Phys.* **2015**, *17*, 25333–25341. [CrossRef]
18. Liu, J.; Wang, B.; Li, Z.; Wu, Z.; Zhu, K.; Zhuang, J.; Xi, Q.; Hou, Y.; Chen, J.; Cong, M.; et al. Photo-Fenton reaction and H_2O_2 enhanced photocatalytic activity of α-Fe_2O_3 nanoparticles obtained by a simple decomposition route. *J. Alloy. Compd.* **2019**, *771*, 398–405. [CrossRef]
19. Liu, H.; Tong, M.; Zhu, K.; Liu, H.; Chen, R. Preparation and photo-fenton degradation activity of α-Fe_2O_3 nanorings obtained by adding $H_2PO_4^-$, SO_4^{2-}, and citric acid. *Chem. Eng. J.* **2020**, *382*, 123010. [CrossRef]
20. Jiang, J.; Gao, J.; Li, T.; Chen, Y.; Wu, Q.; Xie, T.; Lin, Y.; Dong, S. Visible-light-driven photo-Fenton reaction with α-Fe_2O_3/BiOI at near neutral pH: Boosted photogenerated charge separation, optimum operating parameters and mechanism insight. *J. Colloid Interface Sci.* **2019**, *554*, 531–543. [CrossRef]
21. Ren, B.; Miao, J.; Xu, Y.; Zhai, Z.; Dong, X.; Wang, S.; Zhang, L.; Liu, Z. A grape-like N-doped carbon/CuO-Fe_2O_3 nanocomposite as a highly active heterogeneous Fenton-like catalyst in methylene blue degradation. *J. Clean. Prod.* **2019**, *240*, 118143. [CrossRef]
22. Bai, J.; Xu, H.; Chen, G.; Lv, W.; Ni, Z.; Wang, Z.; Yang, J.; Qin, H.; Zheng, Z.; Li, X. Facile fabrication of α-Fe_2O_3/porous g-C_3N_4 heterojunction hybrids with enhanced visible-light photocatalytic activity. *Mater. Chem. Phys.* **2019**, *234*, 75–80. [CrossRef]
23. Sun, S.; Ji, C.; Wu, L.; Chi, S.; Qu, R.; Li, Y.; Lu, Y.; Sun, C.; Xue, Z. Facile one-pot construction of α-Fe_2O_3/g-C_3N_4 heterojunction for arsenic removal by synchronous visible light catalysis oxidation and adsorption. *Mater. Chem. Phys.* **2017**, *194*, 1–8. [CrossRef]
24. Hao, Q.; Mo, Z.; Chen, Z.; She, X.; Xu, Y.; Song, Y.; Ji, H.; Wu, X.; Yuan, S.; Xu, H.; et al. 0D/2D Fe_2O_3 quantum dots/g-C_3N_4 for enhanced visible-light-driven photocatalysis. *Colloids Surf. A Physicochem. Eng. Asp.* **2018**, *541*, 188–194. [CrossRef]
25. Zhou, L.; Wang, L.; Zhang, J.; Lei, J.; Liu, Y. Well-Dispersed Fe_2O_3 Nanoparticles on g-C_3N_4 for Efficient and Stable Photo-Fenton Photocatalysis under Visible-Light Irradiation. *Eur. J. Inorg. Chem.* **2016**, *2016*, 5387–5392. [CrossRef]
26. Vayssieres, L.; Beermann, N.; Lindquist, S.-E.; Hagfeldt, A. Controlled Aqueous Chemical Growth of Oriented Three-Dimensional Crystalline Nanorod Arrays: Application to Iron(III) Oxides. *Chem. Mater.* **2001**, *13*, 233–235. [CrossRef]
27. Yan, S.C.; Li, Z.S.; Zou, Z.G. Photodegradation Performance of g-C_3N_4 Fabricated by Directly Heating Melamine. *Langmuir* **2009**, *25*, 10397–10401. [CrossRef]
28. Liu, Q.; Chen, C.; Yuan, G.; Huang, X.; Lü, X.; Cao, Y.; Li, Y.; Hu, A.; Lu, X.; Zhu, P. Morphology-controlled α-Fe_2O_3 nanostructures on FTO substrates for photoelectrochemical water oxidation. *J. Alloy. Compd.* **2017**, *715*, 230–236. [CrossRef]
29. Raja, K.; Mary Jaculine, M.; Jose, M.; Verma, S.; Prince, A.A.M.; Ilangovan, K.; Sethusankar, K.; Jerome Das, S. Sol–gel synthesis and characterization of α-Fe_2O_3 nanoparticles. *Superlattices Microstruct.* **2015**, *86*, 306–312. [CrossRef]
30. Thomas, A.; Fischer, A.; Goettmann, F.; Antonietti, M.; Müller, J.-O.; Schlögl, R.; Carlsson, J.M. Graphitic carbon nitride materials: Variation of structure and morphology and their use as metal-free catalysts. *J. Mater. Chem.* **2008**, *18*, 4893–4908. [CrossRef]
31. Qiao, F.; Wang, J.; Ai, S.; Li, L. As a new peroxidase mimetics: The synthesis of selenium doped graphitic carbon nitride nanosheets and applications on colorimetric detection of H_2O_2 and xanthine. *Sens. Actuators B Chem.* **2015**, *216*, 418–427. [CrossRef]
32. Su, S.; Liu, Y.; Liu, X.; Jin, W.; Zhao, Y. Transformation pathway and degradation mechanism of methylene blue through β-FeOOH@GO catalyzed photo-Fenton-like system. *Chemosphere* **2019**, *218*, 83–92. [CrossRef] [PubMed]
33. Liu, W.; Li, Y.; Liu, F.; Jiang, W.; Zhang, D.; Liang, J. Visible-light-driven photocatalytic degradation of diclofenac by carbon quantum dots modified porous g-C_3N_4: Mechanisms, degradation pathway and DFT calculation. *Water Res.* **2019**, *151*, 8–19. [CrossRef] [PubMed]
34. Abou-Gamra, Z.M.; Ahmed, M.A. Synthesis of mesoporous TiO_2–curcumin nanoparticles for photocatalytic degradation of methylene blue dye. *J. Photochem. Photobiol. B Biol.* **2016**, *160*, 134–141. [CrossRef]
35. Chauhan, R.; Kumar, A.; Pal Chaudhary, R. Photocatalytic degradation of methylene blue with Cu doped ZnS nanoparticles. *J. Lumin.* **2014**, *145*, 6–12. [CrossRef]

36. Jing, H.-P.; Wang, C.-C.; Zhang, Y.-W.; Wang, P.; Li, R. Photocatalytic degradation of methylene blue in ZIF-8. *RSC Adv.* **2014**, *4*, 54454–54462. [CrossRef]
37. Atout, H.; Álvarez, M.G.; Chebli, D.; Bouguettoucha, A.; Tichit, D.; Llorca, J.; Medina, F. Enhanced photocatalytic degradation of methylene blue: Preparation of TiO_2/reduced graphene oxide nanocomposites by direct sol-gel and hydrothermal methods. *Mater. Res. Bull.* **2017**, *95*, 578–587. [CrossRef]
38. Gupta, V.K.; Saleh, T.A.; Pathania, D.; Rathore, B.S.; Sharma, G. A cellulose acetate based nanocomposite for photocatalytic degradation of methylene blue dye under solar light. *Ionics* **2015**, *21*, 1787–1793. [CrossRef]
39. Yang, Y.; Xu, L.; Wang, H.; Wang, W.; Zhang, L. TiO_2/graphene porous composite and its photocatalytic degradation of methylene blue. *Mater. Des.* **2016**, *108*, 632–639. [CrossRef]
40. Wang, Z.; Luo, C.; Zhang, Y.; Gong, Y.; Wu, J.; Fu, Q.; Pan, C. Construction of hierarchical TiO_2 nanorod array/graphene/ZnO nanocomposites for high-performance photocatalysis. *J. Mater. Sci.* **2018**, *53*, 15376–15389. [CrossRef]
41. Niu, X.; Yan, W.; Shao, C.; Zhao, H.; Yang, J. Hydrothermal synthesis of Mo-C co-doped TiO_2 and coupled with fluorine-doped tin oxide (FTO) for high-efficiency photodegradation of methylene blue and tetracycline: Effect of donor-acceptor passivated co-doping. *Appl. Surf. Sci.* **2019**, *466*, 882–892. [CrossRef]
42. Wu, F.; Li, X.; Liu, W.; Zhang, S. Highly enhanced photocatalytic degradation of methylene blue over the indirect all-solid-state Z-scheme g-C_3N_4-RGO-TiO_2 nanoheterojunctions. *Appl. Surf. Sci.* **2017**, *405*, 60–70. [CrossRef]
43. Ma, D.; Wu, J.; Gao, M.; Xin, Y.; Sun, Y.; Ma, T. Hydrothermal synthesis of an artificial Z-scheme visible light photocatalytic system using reduced graphene oxide as the electron mediator. *Chem. Eng. J.* **2017**, *313*, 1567–1576. [CrossRef]
44. She, X.; Wu, J.; Xu, H.; Zhong, J.; Wang, Y.; Song, Y.; Nie, K.; Liu, Y.; Yang, Y.; Rodrigues, M.-T.F.; et al. High Efficiency Photocatalytic Water Splitting Using 2D α-Fe_2O_3/g-C_3N_4 Z-Scheme Catalysts. *Adv. Energy Mater.* **2017**, *7*, 1700025. [CrossRef]
45. Xu, Q.; Zhu, B.; Jiang, C.; Cheng, B.; Yu, J. Constructing 2D/2D Fe_2O_3/g-C_3N_4 Direct Z-Scheme Photocatalysts with Enhanced H_2 Generation Performance. *Sol. RrL* **2018**, *2*, 1800006. [CrossRef]
46. Jiang, Z.; Wan, W.; Li, H.; Yuan, S.; Zhao, H.; Wong, P.K. A Hierarchical Z-Scheme α-Fe_2O_3/g-C_3N_4 Hybrid for Enhanced Photocatalytic CO_2 Reduction. *Adv. Mater.* **2018**, *30*, 1706108. [CrossRef]
47. Shaban, M.; Abukhadra, M.R.; Ibrahim, S.S.; Shahien, M.G. Photocatalytic degradation and photo-Fenton oxidation of Congo red dye pollutants in water using natural chromite—Response surface optimization. *Appl. Water Sci.* **2017**, *7*, 4743–4756. [CrossRef]